# Supporting Information

## A Caging Strategy for Tuning the Magneto-Optical Properties of Cobalt Ferrite using a Single Plasmonic Nanoparticle

M. Testa-Anta, A. Sousa-Castillo, A. López-Ortega, M. A. Correa-Duarte, A. García-Martín, P. Vavassori and V. Salgueiriño*

[a.] *Departamento de Física Aplicada, Universidade de Vigo, 36310 Vigo (Spain). E-mail: vsalgue@uvigo.es*
[b.] *CINBIO, Universidade de Vigo, 36310 Vigo (Spain).*
[c.] *Instituto de Nanociencia, Nanotecnología y Materiales Moleculares and Dpto. de Física Aplicada, Universidad de Castilla-La Mancha, Campus Fábrica de Armas, 45071 Toledo (Spain).*
[d.] *Instituto de Micro y Nanotecnología IMN-CNM, CSIC, CEI UAM+CSIC, Isaac Newton 8, Tres Cantos, Madrid 28760, Madrid (Spain).*
[e.] *CIC-Nanogune, 20018 Donostia-San Sebastián and IKERBASQUE, 48013 Bilbao (Spain)*

### Experimental Section

*Chemicals.* Tetrachloroauric(III) acid trihydrate ($HAuCl_4.3H_2O$, 99%), sodium citrate tribasic dihydrate ($Na_3C_6H_5O_7.2H_2O$, ≥98%), cobalt(II) chloride hexahydrate ($CoCl_2.6H_2O$, 98%), iron(III) chloride hexahydrate ($FeCl_3.6H_2O$, ≥99%), iron(III) nitrate nonahydrate ($Fe(NO_3)_3.9H_2O$, ≥98%), sodium hydroxide (NaOH, ≥97%), hydrochloric acid (HCl, 37%), nitric acid ($HNO_3$, 64-66%), potassium persulfate ($K_2S_2O_8$, 99.99%), styrene (≥99%), poly(diallyldimethylammonium chloride) (PDADMAC) (Mw < 100.000), poly(sodium 4-styrenesulfonate) (PSS) (Mw ~ 70.000), sodium chloride (NaCl, ≥99.5%), ammonium hydroxide solution ($NH_4OH$, 28.0-30.0% wt. $NH_3$ in water) and tetraethyl orthosilicate (TEOS, 98%) were purchased from Sigma-Aldrich. Sodium lauryl sulfate (95%) was supplied by Scharlab. All chemicals were used as received without further purification. Pure grade ethanol and Milli-Q water were used in all the preparations.

*Synthesis of 20 and 60 nm Au nanoparticles.* 20 nm citrate-stabilized gold nanoparticles were prepared according to the classical method described by Turkevich,[1] by which a stable dispersion of nanoparticles with a size distribution centered at 20.3 ± 3 nm was achieved. Alternatively, 60 nm-sized gold nanoparticles were synthesized following a kinetically controlled seed-mediated growth strategy similar to that reported by Bastús *et al.*,[2] thereby achieving an average diameter of 60.3 (± 5) nm.

*Synthesis of Au-PS dimers.* Using the previous gold nanoparticles as seeds, polystyrene (PS) spheres were grown up to an average size of 450 (± 10) nm, to form Au-PS dimers. To this end, sodium lauryl sulfate (0.028 g, 0.092 mmol) was dissolved in a mixture of 25 mL of ethanol and 3 mL of water. The reaction mixture was then heated to 70 ºC under nitrogen flow, and potassium persulfate (0.024 g, 0.089 mmol) (dissolved in 3 mL of water) and styrene (420 µL, 3.62 mmol) were subsequently injected under magnetic stirring. After 5 minutes were elapsed, 3 mL of a concentrated gold nanoparticles aqueous dispersion were slowly injected and the reaction was allowed to continue for 8 hours. The as-synthesized Au-PS dimers were collected via centrifugation (6000 rpm, 20 min) and washed several times with ethanol.

*Synthesis and deposition of $CoFe_2O_4$ nanoparticles onto Au-PS dimers.* 16 nm cobalt ferrite nanoparticles were synthesized following a method described elsewhere,[3] by which a stable aqueous dispersion of $CoFe_2O_4$ nanoparticles with an average diameter of 16 (± 6) nm was obtained. Once synthesized, the cobalt ferrite nanoparticles were driven onto the Au-PS dimers by using the well-established Layer-by-Layer (LbL) technique.[4] Accordingly, the Au-PS dimers were first primed with two layers of polyelectrolytes, PDADMAC and PSS, thus providing a negatively charged and smooth surface that assists the subsequent uniform deposition of the cationic cobalt ferrite nanoparticles synthesized. The polyelectrolyte-coated Au-PS dimers were prepared by taking the Au-PS dimers sedimented from 3.125 mL of suspension (4 mg/mL), adding 25 mL of PDADMAC (1 mg $mL^{-1}$, containing 0.5 M NaCl) solution, waiting 30 min for absorption, and then removing the excess of polyelectrolyte by four subsequent centrifugation/wash (6000 rpm, 20 min) cycles. PSS (1 mg $mL^{-1}$, containing 0.5 M NaCl) was deposited onto the PDADMAC-coated dimers using the same procedure. $CoFe_2O_4$ nanoparticles were then deposited by adding 400 µL of the $CoFe_2O_4$ sol (~0.05 M) to the polyelectrolyte-coated dimers (dispersed in 10 mL of water), and water was added to make a total volume of 70.4 mL. The $CoFe_2O_4$ nanoparticles were allowed to adsorb for 20 min, and the excess of nanoparticles was removed by five repeated centrifugation/wash (6000 rpm, 20

min) cycles. The sample was finally dispersed in 25 mL of water. Analogous process was followed for the deposition of the cobalt ferrite nanoparticles onto PS spheres.

*Silica coating and formation of the hollow nanostructures*. 5 mg of the $CoFe_2O_4$-coated Au-PS dimers (dispersed in 1 mL of water) were added to 70 mL of a 4.2% (v/v) ammonia/ethanol solution, following the Stöber method.[5] The mixture was then stirred for 10 min. After that, 0.375 mL of a 10% (v/v) TEOS/ethanol solution were added dropwise. The mixture was left under mechanical stirring for 2 h. The excess of reagents was removed by three centrifugation-redispersion (4500 rpm, 20 min) cycles with a 50% (v/v) ethanol/water solution, letting finally the sample dry. Hollow silica microcapsules were eventually obtained by calcination of the PS component present in the composites, at 600 ºC for 4 h, which also leads to the rearrangement of the crystalline structure of the magnetic nanoparticles.

*Characterization.* Samples for TEM were prepared by depositing them upon a carbon-coated copper grid. TEM measurements were performed on a JEOL JEM 1010 microscope operating at 100 kV. Size histograms were obtained by manual counting over 100 particles, with size distributions fitted to Gauss functions (normal distributions). UV−Vis absorbance or transmittance spectra were recorded on a HP8453 UV−Vis spectrophotometer fitted with a thermostated holder and collected from a 1-cm pathlength quartz cuvette. Magnetic measurements were performed using a PPMS Quantum Design equipped with VSM magnetometry. Field-dependent magnetization curves were obtained applying an external field up to 6 T at 300 K. Raman spectra were obtained with a Renishaw inVia Reflex confocal system. Experiments were conducted at room temperature using three laser excitation wavelengths: a 532 nm frequency doubled Nd:YAG/Nd:$YVO_4$ diode, a 633 nm He-Ne laser and a 785 nm NIR diode laser. The laser beam was focused onto the sample by a 20x objective with a numerical aperture (NA) value of 0.40, and the Raman spectra were registered in backscattering geometry with a high-resolution grating of 1800 grooves/mm or 1200 grooves/mm. The spectra were obtained over an acquisition time of 120 seconds, one

accumulation and under variable laser powers (ranging from 0.16 to 55 mW). Magneto-Optical characterization has been performed in polar Faraday configuration (*i.e.*, light transmitted through the sample with the applied magnetic field perpendicular to the surface of the sample) in the 400 to 860 nm spectral range. Faraday ellipticity and rotation angles have been measured at different wavelengths by impinging with a linearly polarized beam and revealing the polarization of the transmitted beam after passing it through a photoelastic phase modulator and a polarizer before detection. Two lock-in amplifiers were used to filter the signal at the modulation frequency and at twice the modulation frequency in order to retrieve Faraday ellipticity and rotation simultaneously.[6] Faraday rotation and ellipticity angles have been measured at saturation magnetization (0.7 T) for ferrimagnetic samples (C-Ref, C-Au20, C-Au60 and $CoFe_2O_4$) and at 0.45 T for diamagnetic samples (Au20 and Au60). Magneto-optical activity (MOA) is defined as the modulus of the complex Faraday angle.

*Theoretical Simulation Methods.* To obtain theoretically the optical and magneto-optical properties of the samples under study, we have made use of the Magneto-Optical version of the Discrete Dipole Approximation or MO-DDA,[7] by which each $CoFe_2O_4$ (16 nm in diameter) and Au (20 or 60 nm in diameter) is represented as a single electric dipole. The optical and magneto-optical response can therefore be determined by the magnitude and orientation of these dipoles, that is, considering the result of the full electromagnetic interaction between the impinging plane wave (linearly polarized along $u_x$ and propagating along $u_z$) and the scattering produced in each of them (as described in [7]). To mimic the actual experimental situation where the system is a hollow-core nanoshell decorated with the $CoFe_2O_4$ nanoparticles and a single Au nanoparticle, we have produced a random collection (uniformly distributed) of entities in the shell (as depicted in the sketch in Figure 4a) and one single Au entity located at $u_z$ direction (this predefined choice of the gold location is further rotated to average the effect that the anisotropy induced by the location of the Au has in the optical and magneto-optical properties).

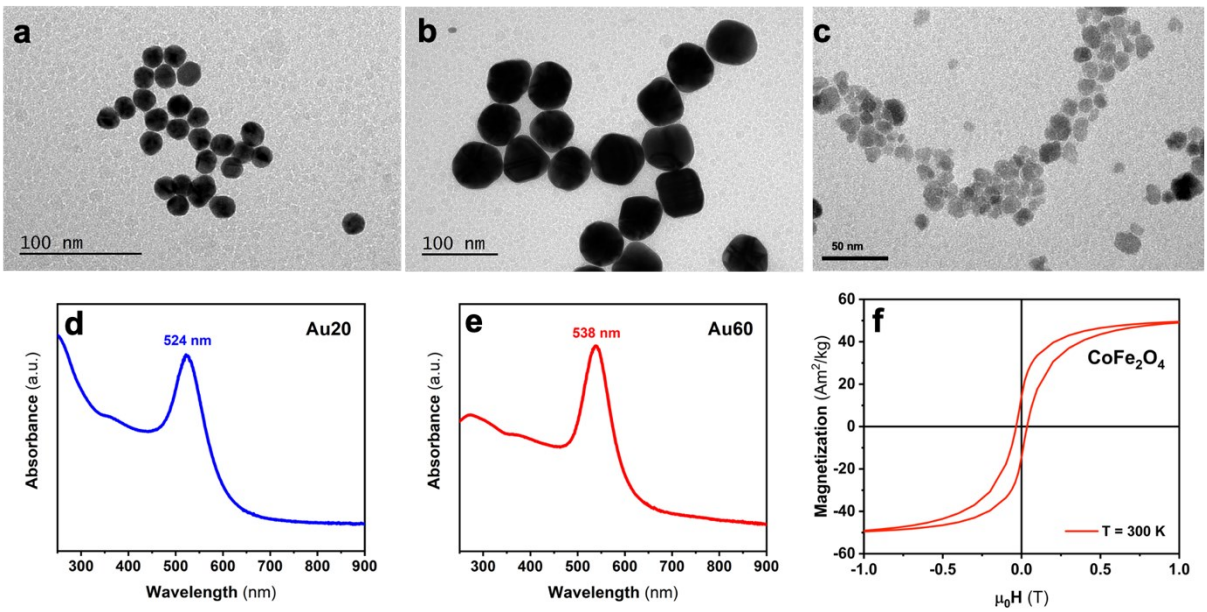


**Figure S1**. TEM images and UV-vis spectra of the 20 nm (a, d) and 60 nm (b, e) gold nanoparticles. TEM characterization of the 16 nm cobalt ferrite nanoparticles (c) and corresponding magnetization *vs* field hysteresis loop registered at 300 K (f).

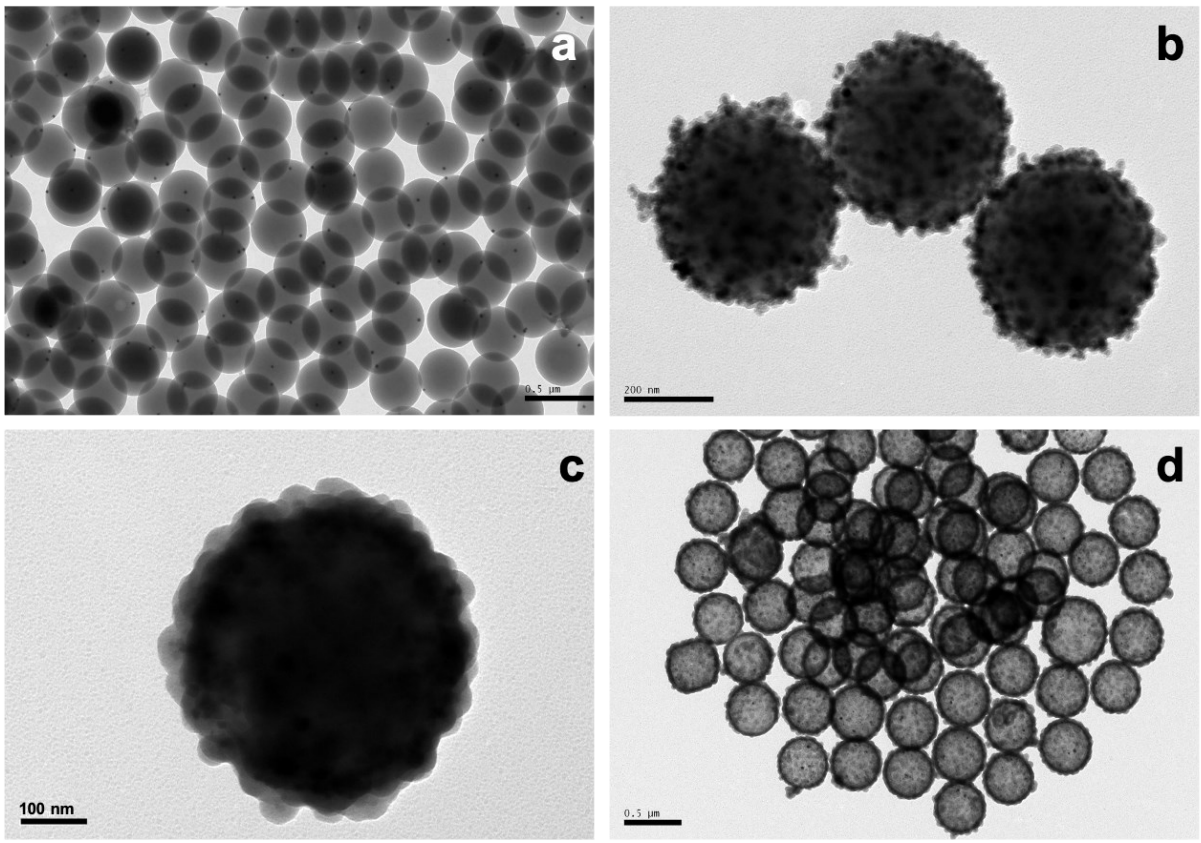


**Figure S2**. TEM images corresponding to the different intermediate steps followed to accomplish the synthesis of the C-Au20 capsules: Au20-PS dimers after inducing the growth of the polystyrene spheres using 20 nm gold nanoparticles as seeds (a), deposition of $CoFe_2O_4$ nanoparticles onto the Au20-PS dimers using the LbL self-assembly technique (b), homogenous precipitation of a 30 nm silica shell onto the cobalt ferrite-coated Au20-PS dimers, using the Stöber method (c), and calcination of the PS component in order to promote the formation of hollow capsules and removing of organic compounds (d).

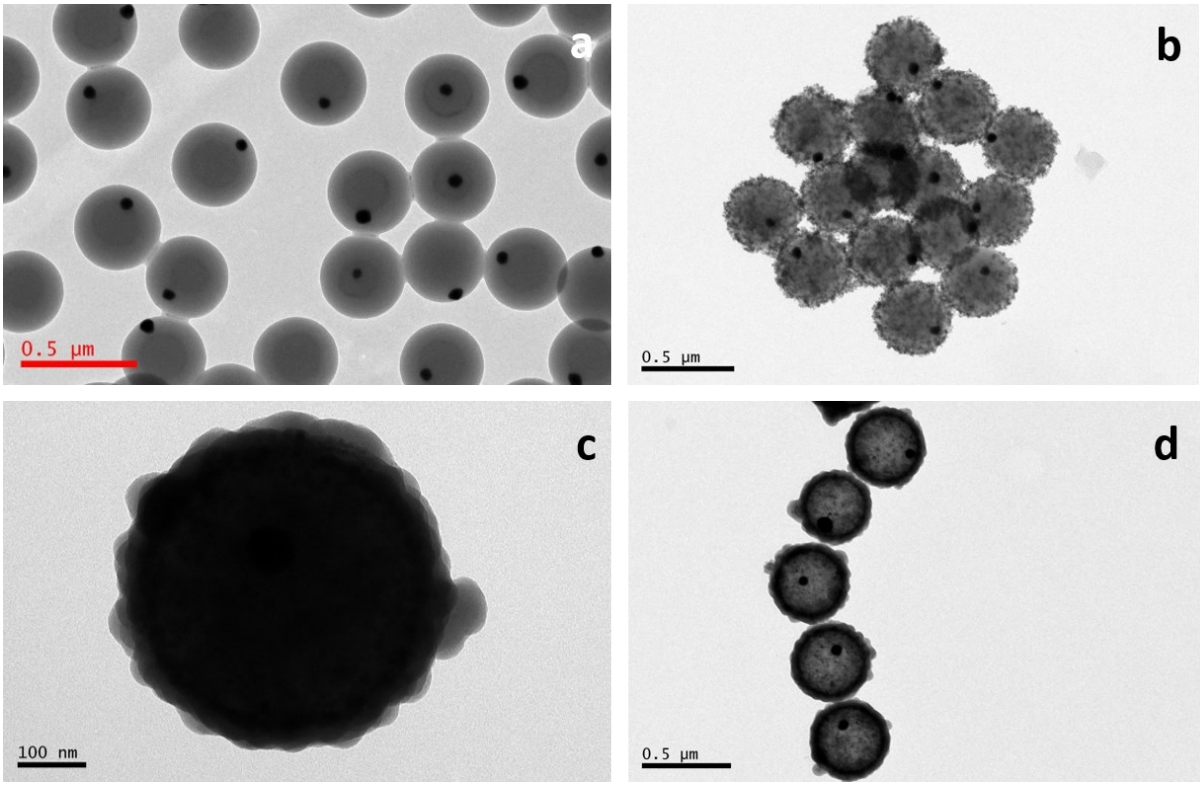


**Figure S3**. TEM images corresponding to the different intermediate steps followed to accomplish the synthesis of the C-Au60 capsules: Au60-PS dimers after inducing the growth of the polystyrene spheres using 60 nm gold nanoparticles as seeds (a), deposition of $CoFe_2O_4$ nanoparticles onto the Au60-PS dimers using the LbL self-assembly technique (b), homogenous precipitation of a 30 nm silica shell onto the cobalt ferrite-coated Au60-PS dimers, using the Stöber method (c), and calcination of the PS component in order to promote the formation of hollow capsules and removing of organic compounds (d).

**Determination of the Faraday rotation and ellipticity**

The magneto-optical Faraday rotation and ellipticity were simultaneously registered by using an intensity method,[6] according to the following equations:

$$\theta_F = \frac{tan\theta \quad \Delta I_{2\omega}}{1.221 I_0 - I_{bias}}, \varepsilon_F = \frac{-tan\theta \quad \Delta I_{\omega}}{1.408\ I_0 - I_{bias}} \text{ (eq. S1)}$$

where $\theta_F$ and $\varepsilon_F$ stand for the Faraday rotation and ellipticity respectively, $\theta$ the extinction angle, $\Delta I_w$ and $\Delta I_{2w}$ are the intensity amplitudes registered as a function the applied magnetic field (at ω and 2ω modulation frequencies, respectively), $I_0$ the average intensity at zero field, and $I_{bias}$ the background intensity contribution.

For the determination of the intensity amplitude $\Delta I$, two different approaches were followed:

- In the case of C-Ref, C-Au20, C-Au60 and $CoFe_2O_4$ samples, the linear contribution responsible for the non-saturation of the intensity at large magnetic fields was subtracted, such that a sigmoid-like signal was obtained. The difference in intensity between the upper and lower saturation regions was taken as $\Delta I$.

- Contrarily, for the Au20 and Au60 samples the intensity displayed a rather linear dependence on the applied magnetic field. Hence, the difference between the intensity corresponding to a 0.43 T and a -0.43 T magnetic field was taken as $\Delta I$. This magnetic field threshold was chosen since it does represent the minimum field required for the saturation of the C-Ref, C-Au20, C-Au60 and $CoFe_2O_4$ samples.

The magneto-optical activity (MOA) has been calculated as the modulus of the complex Faraday angle (whose real and imaginary parts are the Faraday rotation and ellipticity, respectively):

$$MOA = (\theta_F{}^2 + \varepsilon_F{}^2)^{1/2} \qquad (eq. S2)$$

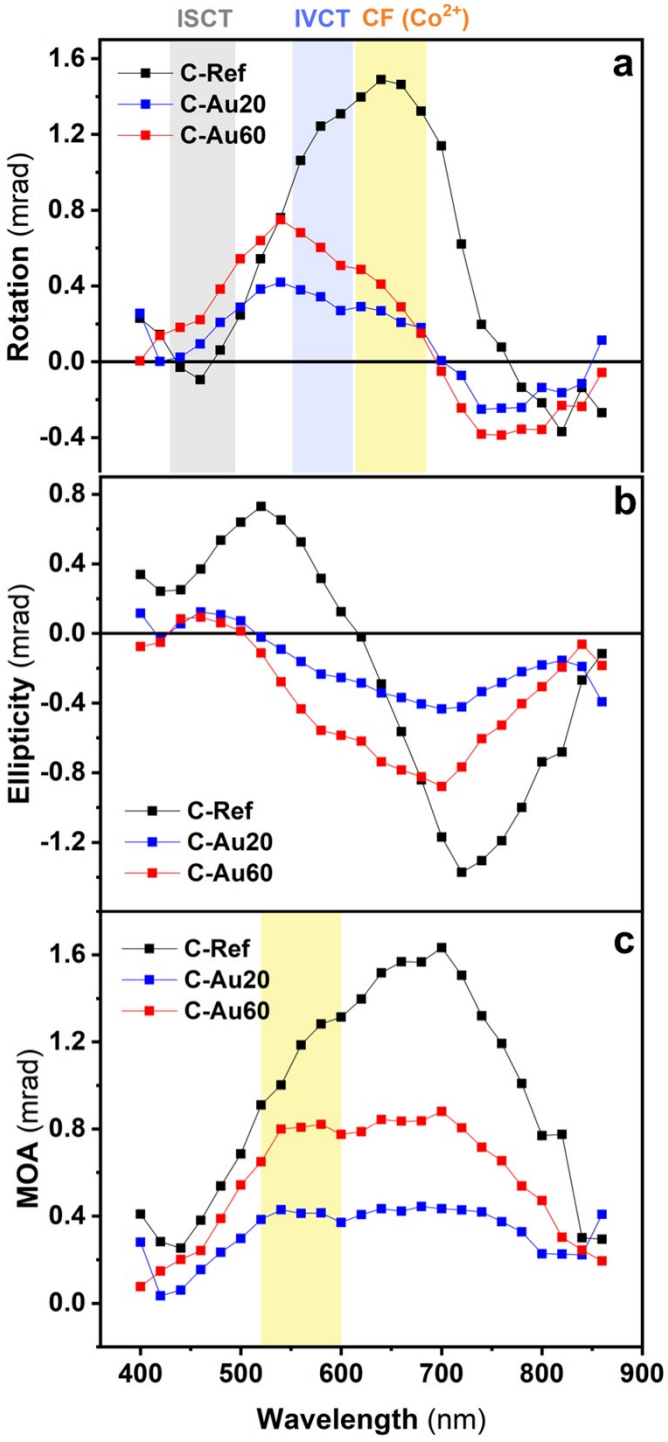


**Figure S4**. Faraday rotation (a), ellipticity (b) and derived magneto-optical activity (MOA) spectra for the three different types of capsules: C-Ref (black), C-Au20 (blue) and C-Au60 (red), recorded in the visible-near infrared spectral range applying a magnetic field up to 0.7 T. For these measurements, the capsules were redispersed in water and drop-casted onto glass

substrates, but with no control over the concentration of the capsules. Pale grey, blue and yellow areas in the Faraday rotation plot indicate the theoretical position of the ISCT, IVCT and CF transitions of the cobalt ferrite and the pale-yellow area in the MOA graph frames the range where it becomes modified.

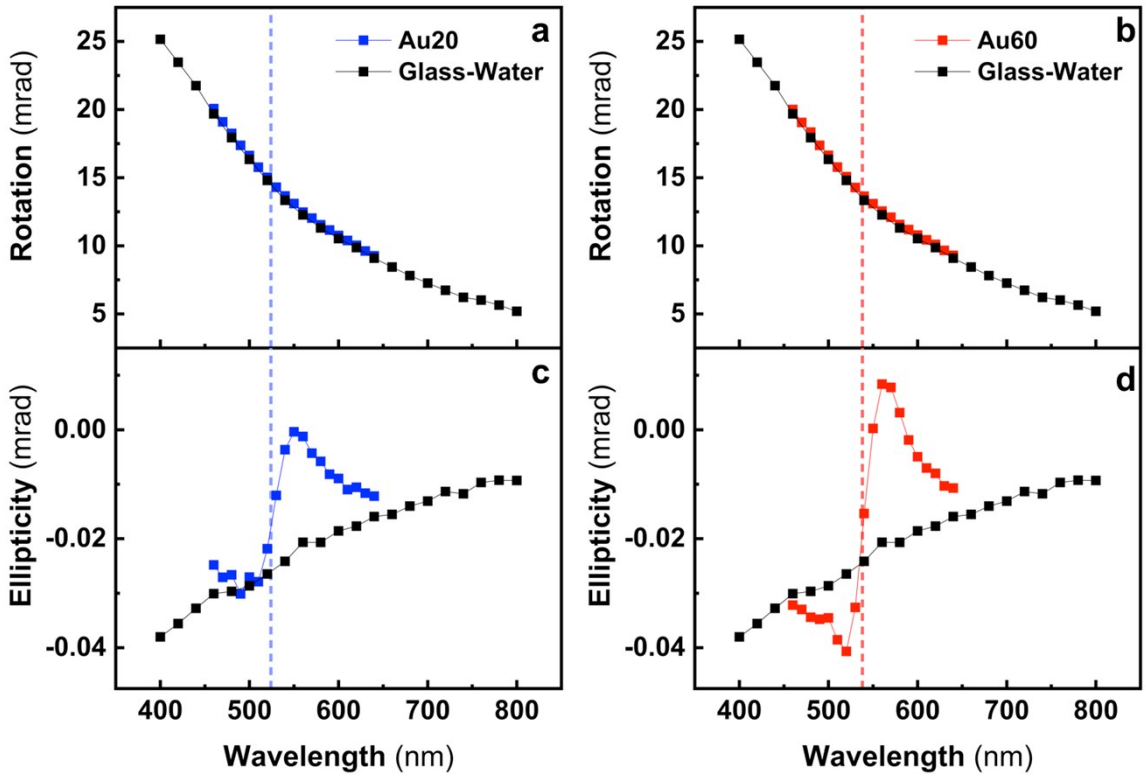


**Figure S5**. Faraday rotation and ellipticity spectra of the 20 nm and 60 nm gold nanoparticles: Au20 (a, b) and Au60 (c, d). All these measurements were performed in solution (in water) using a 1-mm path-length cuvette, and hence, the magneto-optical signal from the cuvette filled with water (referred to as Glass-Water) was registered as reference.

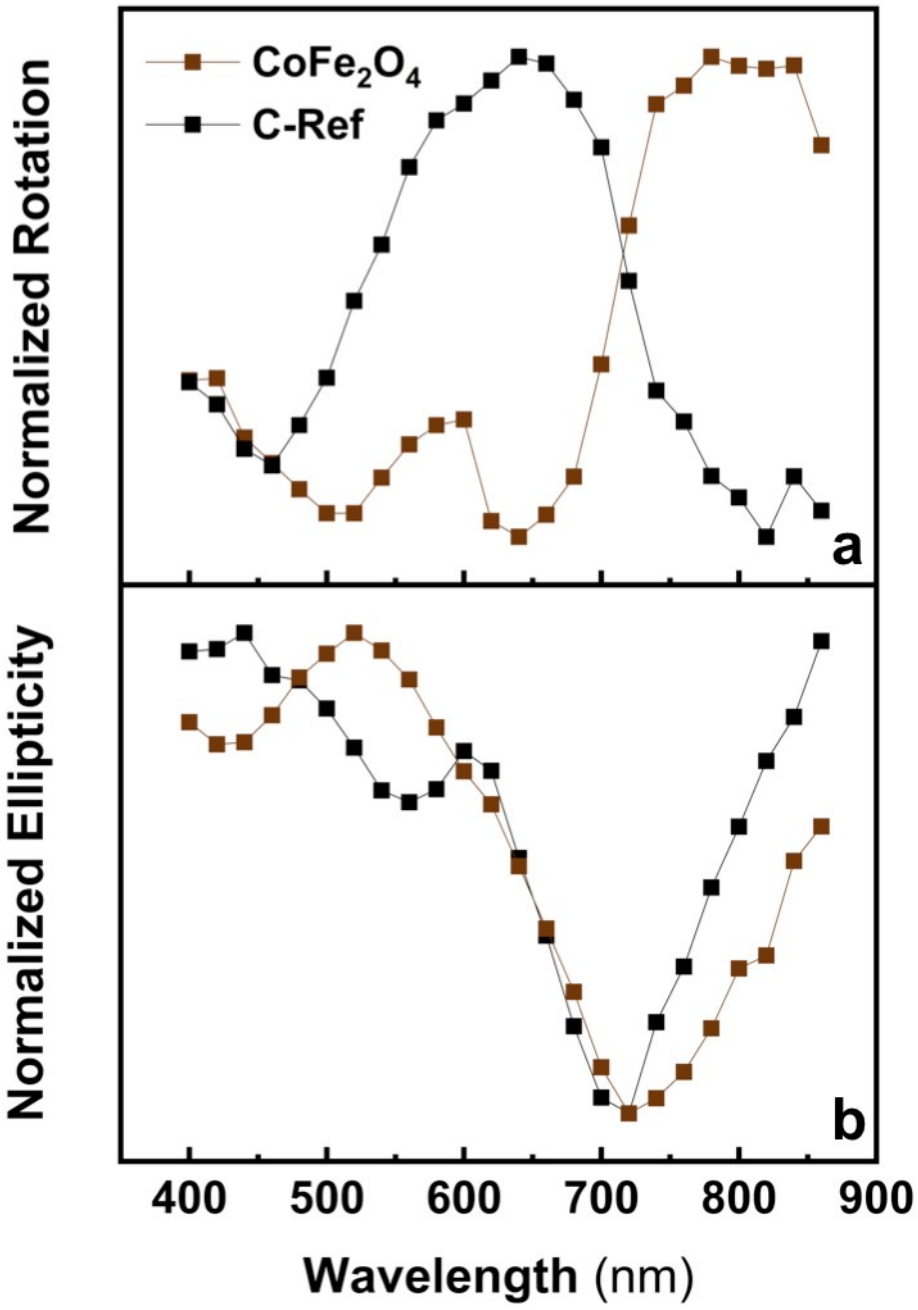


**Figure S6**. Normalized Faraday Rotation (a) and ellipticity (b) spectra of the cobalt ferrite ($CoFe_2O_4$) nanoparticles and of the C-Ref sample (a). Due to their magnetic nature, both samples were redispersed in water and drop-casted onto a glass substrate for these measurements.

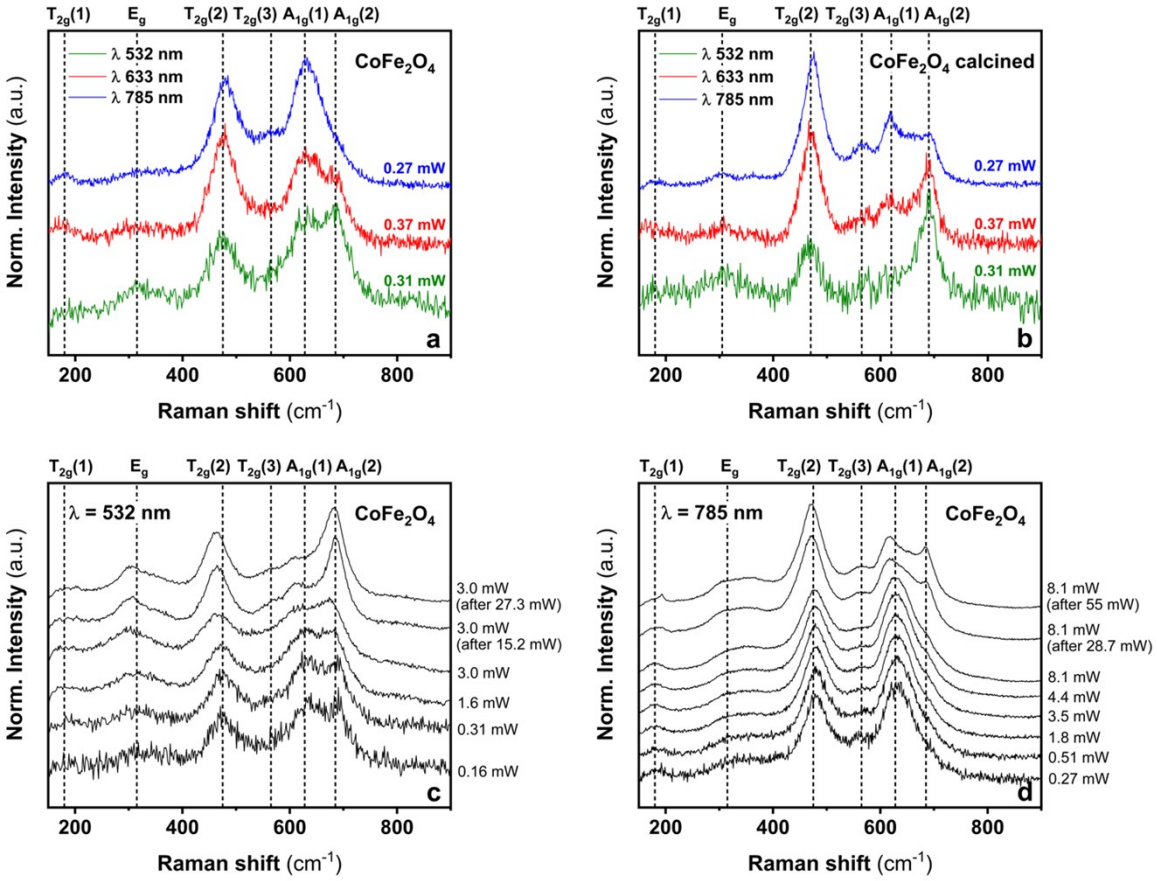


**Figure S7**. Raman spectra of the cobalt ferrite ($CoFe_2O_4$) nanoparticles before (a) and after (b) a calcination process at 600 ºC, using 532, 633 and 785 nm excitation wavelengths while keeping similar values of the laser power. Raman spectra of the as-synthesized cobalt ferrite nanoparticles (i.e. before the calcination process) registered under a 532 (c) or 785 nm (d) excitation wavelength, as a function of the laser power and collected from the same spot in the sample.

Figures S7a and S7b include the Raman spectra of cobalt ferrite nanoparticles before and after calcination, respectively, obtained using three different excitation wavelengths (532, 633 and 785 nm) and a similar laser power in all cases. According to group theory, the cobalt ferrite spinel structure (space group *Fd-3m*) presents the following optical phonon modes:

$$\Gamma = A_{1g}(R) + E_g(R) + T_{1g} + 3T_{2g}(R) + 2A_{2u} + 2E_u + 4T_{1u}(IR) + 2T_{2u}$$

out of which five are Raman active (indicated with *(R)*).

Six main features centered at 180, 315, 475, 565, 628 and 685 $cm^{-1}$ can be observed in the Raman spectra included in Figure S7a, which correspond to the vibrational modes $T_{2g}(1)$, $E_g$,

$T_{2g}(2)$, $T_{2g}(3)$, $A_{1g}(1)$ and $A_{1g}(2)$ respectively. While not that clear in the 785 nm-excitation wavelength spectrum (in blue in figure S7a), the 532 and 633 nm-excitation wavelength spectra can better resolve the $A_{1g}$ phonon mode, which is found to split into two different modes,[8-10] centered at 628 and 685 $cm^{-1}$. In the case of the mixed-valence magnetite ($FeFe_2O_4$), this $A_{1g}$ mode is very intense and symmetric, without visible features of different intensities due to the different positions of iron sites in the inverse spinel structure, owing to its delocalized electronic structure.[11] Conversely, the splitting of the $A_{1g}$ mode observed in the as-synthesized $CoFe_2O_4$ nanoparticles indicates the presence of $Co^{2+}$ cations being incorporated into the spinel structure. This fact is also confirmed by the high intensity registered for the $T_{2g}(2)$ vibrational mode, which has been reported to account solely for the $Co^{2+}$ ions at octahedral sites, since typically overshadowed in the case of $Fe_3O_4$.[12] Paying attention now to the spectra in Figure S7b, stemming from the calcined sample of $CoFe_2O_4$ nanoparticles, we can also observe this splitting of the $A_{1g}$ mode, more clearly in the 633 and 785 nm-excitation wavelength spectra. However, in the calcined sample the intensity ratio between the $A_{1g}(1)$ and $A_{1g}(2)$ modes has changed, being the $A_{1g}(2)$ mode more intense than the $A_{1g}(1)$ (under the 532 and 633 excitation wavelengths). Previous studies in the literature have addressed the origin of the relative intensity between these two $A_{1g}$ components.[13,14] Supported by X-ray Diffraction and Mössbauer spectroscopy, the higher-frequency $A_{1g}$ phonon mode was attributed to the trivalent iron cations at tetrahedral sites, whereas the lower-frequency $A_{1g}$ component was directly correlated to the presence of $Co^{2+}$ cations at the same interstices. Accordingly, the Raman spectra in Figure S7a reveal an important fraction of $Co^{2+}$ ions lying at the tetrahedral sites, as reflected by the high intensity of the $A_{1g}(1)$ mode. This observation becomes particularly pronounced under the 785 nm excitation wavelength, where the $A_{1g}(2)$ mode is completely screened by the $A_{1g}(1)$ mode. Likewise, the reduced intensity for the $T_{2g}(2)$ mode points to a low percentage of $Co^{2+}$ ions at the octahedral voids. Nevertheless, these results suggest that the as-synthesized nanoparticles display a lower inversion degree than that expected for the inverse

cobalt ferrite, likely due to a non-stoichiometric composition. The coexistence of two spinel phases with different stoichiometry cannot be discarded either, since the sample was proven to be non-homogeneous (through multiple scans performed at different spots in the sample). According to this, the predominance of a cobalt-rich spinel with a low degree of inversion would account for the experimental Raman results.

Upon calcination, a redistribution of the $Co^{2+}$ and $Fe^{3+}$ cations within the spinel structure is promoted, given the tendency of the cobalt ferrite to rearrange in an inverse spinel structure ($(Fe^{3+})_A[Co^{2+}Fe^{3+}]_BO_4$)[15] (where A and B denote the tetrahedral and octahedral sites, respectively). Hence, more $Co^{2+}$ cations reallocate in the octahedral sites by simultaneously favoring the insertion of more $Fe^{3+}$ cations into the tetrahedral positions. This reallocation of the $Co^{2+}$ cations in the octahedral sites can be evidenced from the increase in the relative intensity of the $T_{2g}(2)$ mode, as well as from the large decrease in the $A_{1g}(1)$ mode intensity (which implies $Co^{2+}$ cations moving away from the tetrahedral interstices). The incorporation of the trivalent iron cations at the tetrahedral sites is reflected by the concomitant increase in the $A_{1g}(2)$ mode intensity. According to this Raman study, the heat transfer during the calcination process helps to improve the crystallographic arrangement of the cobalt ferrite, given the lower quality expected for nanoparticles synthesized by a co-precipitation method, as in this case.

As an alternative proof of this process taking place, figures S7c and S7d reflect this cationic rearrangement of the iron-cobalt oxide into a more inverse spinel structure, because of the energy transfer and consequent local heating induced by both the 532 and 785 nm-excitation wavelengths as increasing the laser power, respectively. In both cases, the spectra registered after applying the highest laser power onto the as-synthesized nanoparticles match exactly the spectra obtained from the calcined sample under the corresponding wavelengths. This proves that the cation distribution within the spinel structure, and therefore the Raman and magneto-optical signals registered, strongly depend on the thermal history of the sample. It is noteworthy

to mention that, despite the fact that the calcination process is shown to increase the inversion parameter of the cobalt ferrite nanoparticles, some $Co^{2+}$ ions still occupy the tetrahedral sites, as reflected by the presence (though to a much less extent) of the $A_{1g}(1)$ mode in the calcined sample. The possibility of $Co^{2+}$ oxidation to $Co^{3+}$ because of the high temperature employed should be taken as well into account. In line with other studies in the literature, these $Co^{3+}$ ions will preferentially occupy the octahedral sites and promote a $Co^{2+}$ migration from octahedral to tetrahedral sites.[12,16] In any case, the Raman results support the presence of $Co^{2+}$ ions at both tetrahedral and octahedral interstices, ultimately responsible for the crystal-field (CF) and IVCT magneto-optical transitions observed.

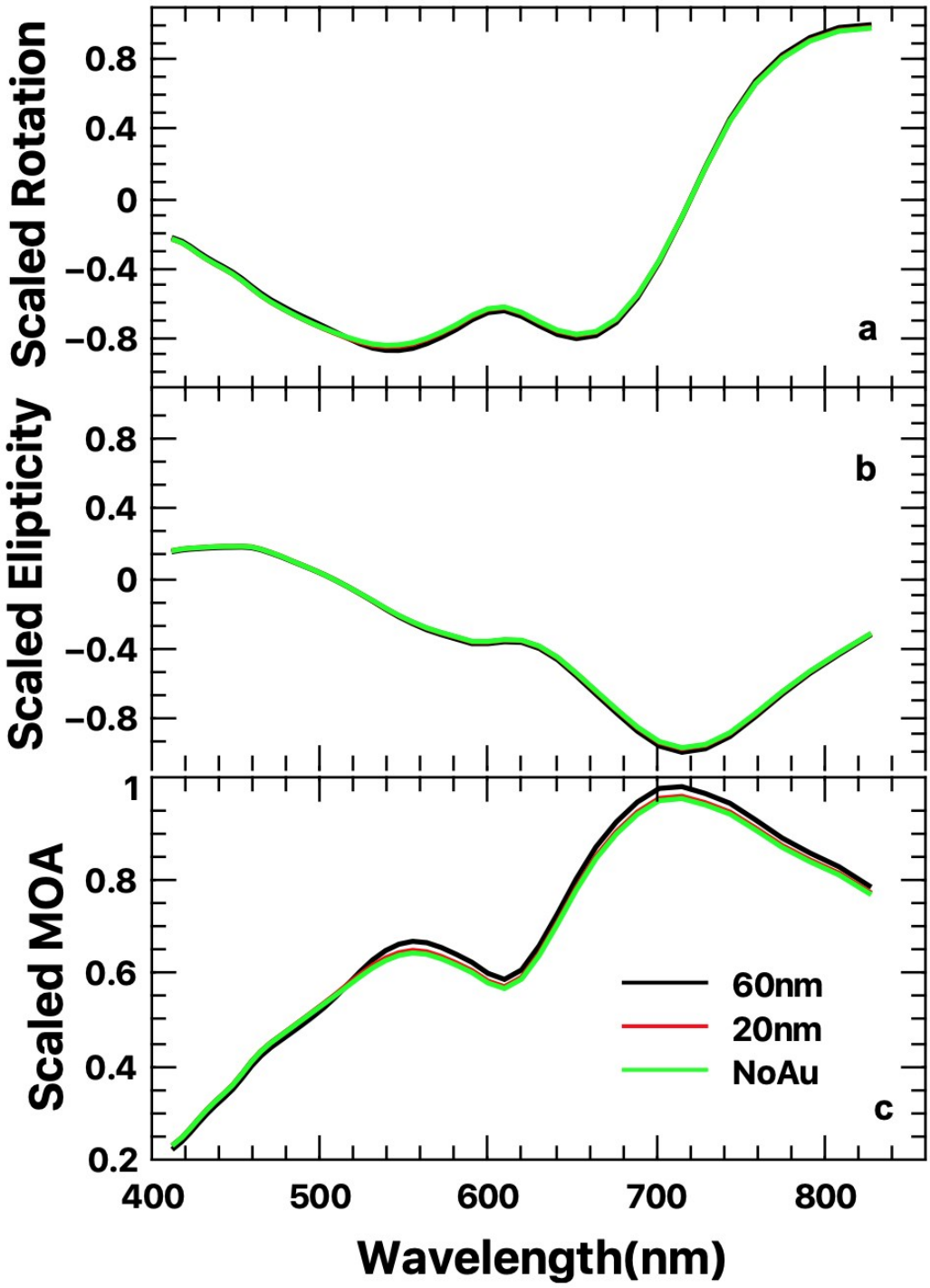


**Figure S8**. Theoretical calculation of the rotation (a), ellipticity (b) and MOA (c) (all normalized) of the three cases considered ("NoAu", "20nm" and "60nm"), taking into account a random collection of 587 nanoparticles of $CoFe_2O_4$ and one nanoparticle of Au, averaged over the angle obtained by aligning the gold particle and the center of the shell, and the impinging light.

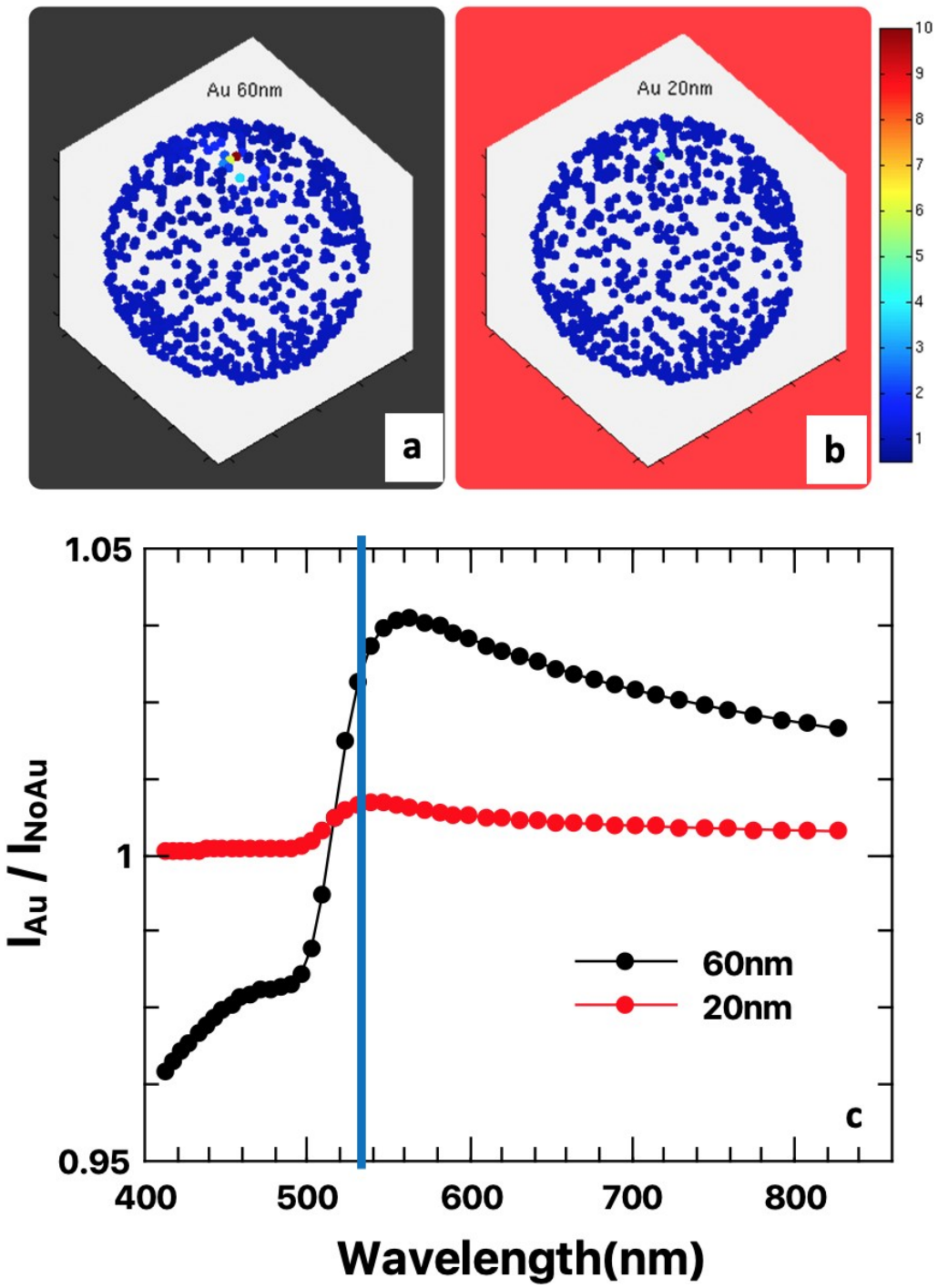


**Figure S9**. Average field intensity (averaged over the alignment with respect to the impinging light) within the ferrite nanoparticles, influenced by a gold particle of 60 nm (a) and 20 nm (b) at a wavelength of 523 nm (see vertical line in c). From the sketches in (a) and (b) and according to the color-coded intensity, it is clear that only cobalt ferrite nanoparticles in very close proximity to the gold one are affected. Further averaging over all nanoparticles, gives the intensity ratio for the two sizes of gold nanoparticles considered. The results in (c) are in consonance with the extinction cross section shown in Fig.4a in the main text.

## References


1. J. Turkevich, P. C. Stevenson, J. Hillier, *Discuss. Faraday Soc.* 1951, **11**, 55-75.
2. N. G. Bastús, J. Comenge, V. Puntes. *Langmuir* 2011, **27**, 11098-11105.
3. J. Wagner, T. Autenrieth, R. Hempelmann. *J. Magn. Magn. Mater.* 2002, **252**, 4-6.
4. E. Donath, G. B. Sukhorukov, F. Caruso, S. A. Davis, H. Möhwald, *Angew. Chem. Int. Ed.*, 1998, **37**, 2201-2205.
5. W. Stöber, A. Fink, E. Bohn, *J. Colloid Interface Sci.* 1968, **26**, 62-69.
6. P. Vavassori. *Appl. Phys. Lett*. 2000, **77**, 1605-1607.
7. N. de Sousa, L. S. Froufe-Pérez, J. J. Sáenz, and A. García-Martín. *Sci. Rep.* 2016, **6**, 30803.
8. N. Fontaiña-Troitiño, M. A. Ramos-Docampo, M. Testa-Anta, B. Rodríguez-González, M. Bañobre-López, L. Bocher, K. P. McKenna, V. Salgueiriño. *J. Mater. Chem. C* 2018, **6**, 12800-12807.
9. M. Testa-Anta, B. Rivas-Murias, V. Salgueiriño. *Adv. Func. Mater.* 2019, **29**, 1900030.
10. J. Preudhomme, P. Tarte. *Spectrochimica Acta* 1971, **27A**, 961-968.
11. A. M. Jubb, H. C. Allen, *ACS Appl. Mater. Interfaces* 2010, **2**, 2804-2812.
12. G. Shemer, E. Tirosh, T. Livneh, G. Markovich. *J. Phys. Chem. C* 2007, **111**, 14334-14338.
13. P. Chandramohan, M. P. Srinivasan, S. Velmurugan, S. V. Narasimban. *J. Solid State Chem.* 2011, **184**, 89-96.
14. N. Bahlawane, P. H. T. Ngamou, V. Vannier, T. Kottke, J. Heberle, K. Kohse-Höinghaus, *Phys. Chem. Chem. Phys.* 2009, **11**, 9224-9232.
15. D. Sharma, N. Khare, *Appl. Phys. Lett.* 2014, **105**, 032404.
16. J. W. D. Martens, W. L. Peeters, H. M. van Noort, M. Erman, *J. Phys. Chem. Solids* 1985, **46**, 411-416.